International Journal of Biological Macromolecules 163 (2020) 2405–2414

Contents lists available at ScienceDirect

International Journal of Biological Macromolecules

journal homepage: http://www.elsevier.com/locate/ijbiomac

Structural modification of NADPH oxidase activator (Noxa 1) by oxidative stress: An experimental and computational study

Pankaj Attri [a,b,*], Jae-Hyun Park [c], Joey De Backer [d], Myeongkyu Kim [c], Ji-Hye Yun [c], Yunseok Heo [c], Sylvia Dewilde [d], Masaharu Shiratani [a], Eun Ha Choi [e], Weontae Lee [c,**], Annemie Bogaerts [b]

[a] Center of Plasma Nano-interface Engineering, Kyushu University, Fukuoka, Japan
[b] Research group PLASMANT, Department of Chemistry, University of Antwerp, Belgium
[c] Department of Biochemistry, College of Life Science & Biotechnology, Yonsei University, 134 Shinchon-Dong, Seodaemoon-Gu, Seoul 120-749, Republic of Korea
[d] Research Group PPES, Department of Biomedical Sciences, University of Antwerp, Universiteitsplein 1, Wilrijk, 1610 Antwerp, Belgium
[e] Department of Electrical and Biological Physics, Kwangwoon University, Seoul 01897, Republic of Korea

ARTICLE INFO

Article history:
Received 10 July 2020
Received in revised form 15 September 2020
Accepted 16 September 2020
Available online 19 September 2020

Keywords:
Noxa1 SH3
Oxidative stress
X-ray crystallography
MD simulations

ABSTRACT

NADPH oxidases 1 (NOX1) derived reactive oxygen species (ROS) play an important role in the progression of cancer through signaling pathways. Therefore, in this paper, we demonstrate the effect of cold atmospheric plasma (CAP) on the structural changes of Noxa1 SH3 protein, one of the regulatory subunits of NOX1. For this purpose, firstly we purified the Noxa1 SH3 protein and analyzed the structure using X-ray crystallography, and subsequently, we treated the protein with two types of CAP reactors such as pulsed dielectric barrier discharge (DBD) and Soft Jet for different time intervals. The structural deformation of Noxa1 SH3 protein was analyzed by various experimental methods (circular dichroism, fluorescence, and NMR spectroscopy) and by MD simulations. Additionally, we demonstrate the effect of CAP (DBD and Soft Jet) on the viability and expression of NOX1 in A375 cancer cells. Our results are useful to understand the structural modification/oxidation occur in protein due to reactive oxygen and nitrogen (RONS) species generated by CAP.

1. Introduction

NADPH oxidase (NOX) enzymes produce superoxide ($O_2^{\bullet -}$) that has many physiological functions in cells, such as cell differentiation, growth and proliferation, embryonic development, and tissue regeneration and development [1–3]. Besides, it was reported that NOX-derived reactive oxygen species (ROS) play a role in cancer development and metastasis [4,5]. Various members of the NOX family, namely NOX1–5, Duox1 and Duox2, are present in tissues [6–8]. The interaction between Nox organizer 1 (Noxo1) and Nox activator 1 (Noxa1 SH3) is required for $O_2^{\bullet -}$ formation by NOX1, as shown in Fig. 1a [9]. Our group previously showed that the SH3 domain of Noxa1 SH3 interacts with the C-terminal region of Noxo1 in the NOX1 complex, see Fig. 1b [9]. However, there is no information about the structural changes in Noxa1 SH3 due to oxidative stress, as produced by cold atmospheric plasma (CAP) during cancer cell treatment.

CAP has attracted much attention in recent years, particularly in biomedical applications, for instance, for bacterial disinfection, cancer treatment and wound healing [10–18]. It was reported that CAP can induce cell death in various types of cancer cells, namely colon cancer, melanoma, cervical cancer, glioma, multiple myeloma; and many more [19]. However, the possible mechanism of the CAP action for cancer treatment is still not entirely clear. It is generally accepted that reactive oxygen and nitrogen species (RONS) produced by CAP react with cancer cells, resulting in its anticancer effect. Bauer et al. suggested that transformed cells express membrane-associated NOX1 in large concentrations, which gives rise to the increase in RONS concentrations in cancer cells during CAP treatment, resulting in deactivation of proteins like catalase [20]. Hence, protein modification can be possible pathway of the anticancer effect of CAP. CAP modifies the amino acids of proteins, affecting the protein structure and function, which results in changes in the secondary and/or tertiary structure of the proteins in the presence and absence of co-solvents, as demonstrated for lysozyme [21,22], horseradish peroxidase [23], myoglobin [24,25], α-chymotrypsin [26–28], lipase [29], MTH1180 [30], hemoglobin [24,25,31], and bacteriorhodopsin [32].

In this study, we examined the possible structural changes of Noxa1 SH3 in the presence of oxidative stress generated by Soft Jet and pulsed dielectric barrier discharge (DBD) CAP treatments for different time interval. In principle, protein oxidation can be monitored by specific antibodies. Protein-bound carbonyls are markers of global protein oxidation

* Correspondence to: Pankaj Attri, Center of Plasma Nano-interface Engineering, Kyushu University, Fukuoka, Japan.
** Corresponding author.
E-mail addresses: chem.pankaj@gmail.com (P. Attri), wtlee@yonsei.ac.kr (W. Lee).

https://doi.org/10.1016/j.ijbiomac.2020.09.120
0141-8130/

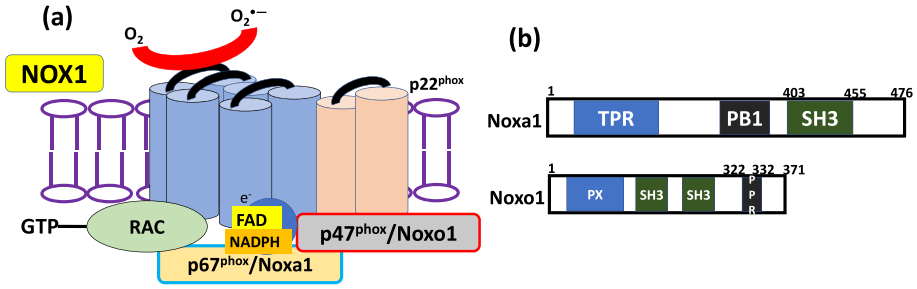

Fig. 1. Schematic representation of the (a) NOX1 protein with domain organization of Noxa1 and Noxo1, and (b) domain of full-length Noxa1 and Noxo1. The SH3 domain of Noxa1 can interact with the C-terminal region containing the proline-rich region (PPR) of Noxo1. Phox/Bem1 domain (PB1); Phox homology domain (PX) [a phospholipid-binding domain]; tetratricopeptide repeat motif (TPR).

in organ homogenates, plasma, isolated proteins, cells, and organelles, as obtained by HPLC, immunoblotting and ELISA [33]. However, such experiments are usually carried out in cells, while we focus on the structural changes in the protein structure in cell-free environment. Therefore, in the present study we focused on the structural change of Noxa1 SH3 protein using circular dichroism (CD), fluorescence and $^{1}H—^{15}N$ NMR spectroscopy. In addition, to determine the stability, flexibility and solvent accessible surface area (SASA), as well as principal component analysis (PCA) in Noxa1 SH3 protein, we performed molecular dynamics (MD) simulations. Finally, we examined cancer cell death by flow cytometry, as well as the expression of NOX1 using western blotting in A375 cancer cells after both types of CAP treatment, in order to obtain insight in the possible pathway of plasma-induced cancer cell death.

2. Material and methods

2.1. Purification and crystallization of Noxa1 SH3

Noxa1 SH3 was cloned as TRX (thioredoxin)-His (histidine) fusion into pET-32a vector and expressed in *E. coli* BL21 (DE3) cells by addition of 1 mM IPTG (isopropyl β-D-1-thiogalactopyranoside) at $OD_{600} = 0.6$. Further cultivation was performed for 16 h at 25 °C. The cells were lysed by sonication in 25 mM sodium phosphate buffer (NaPi), pH 7.5, 300 mM NaCl and 5 mM BME (basement membrane extract) supplemented complete protease inhibitor. Noxa1 SH3 was then purified using Ni-immobilized metal affinity chromatography (Ni-IMAC). The bound non-specific protein was washed for a further 10 column volumes in the same buffer containing 50 mM imidazole. The TRX-His-Noxa1 SH3 fusion was eluted in 4 column volumes of the same buffer containing 250 mM imidazole. The eluted protein was dialysed in the presence of His- tobacco etch virus protease. The dialysed sample was passed through Ni-IMAC to isolate Noxa1 SH3 from the mixed solution. Noxa1 SH3 was concentrated till 3 ml using a molecular mass cut-off of 10 K and was loaded onto Superdex 200 16/600 column equilibrated in 10 mM HEPES (4-(2-hydroxyethyl)-1-piperazineethanesulfonic acid), pH 6.8, 100 mM NaCl, 2 mM DTT (dithiothreitol), 0.01% NaN_3. The protein peak fractions were collected and concentrated to 15 mg/ml for crystallization. Crystals were grown at 16 °C using the sitting drop (vapor diffusion) method in MRC2 plate. The protein was mixed in a 1:1 volume ratio with reservoir solution composed of 100 mM HEPES, pH 7.5, 200 mM magnesium chloride hexahydrate and 25% PEG (poly (ethylene glycol)) 3350. Crystals appeared within 2 days and reached a maximum size after 1 week.

2.2. Data collection and structure determination

The cryopreserved crystals were obtained by soaking the crystals in reservoir solution composed of 100 mM HEPES, pH 7.5, 200 mM magnesium chloride hexahydrate and 25% PEG 3350 supplemented 17% ethylene glycol. A single cryopreserved Noxa1 SH3 crystal was used to solve the structure. The diffraction data of Noxa1 SH3 crystal were collected using 0.96 Å single wave X-ray beam with 100 K liquid nitrogen stream on beamline BL1A at the Photon Factory. The collected diffraction data was initially processed using HKL-2000 [34]. The phase was solved by molecular replacement using the program PHASER [35] with modified SH3 domain of MLK3 (PDB ID: 5K28) as template model. Further processing, model building and refinement was performed using the CCP4 suite [36], Phenix [37] and COOT [38] (Table 1).

2.3. NMR spectroscopy

NMR experiments were performed for chain A of Noxa 1 SH3 native and plasma-treated Noxa1 SH3, using Bruker DRX 850 MHz spectrometer equipped with a Cryoprobe™. Backbone assignment was performed using standard backbone experiments at 25 °C, as reported previously [9,30].

2.4. Pulsed DBD and Soft Jet

We performed the experiments with two different CAP sources, i.e., a pulsed dielectric barrier discharge (DBD) and a plasma jet, called "Soft Jet". The DBD plasma source was fabricated in coplanar configuration by using silver electrodes of width = 100 μm and thickness = 5 μm

Table 1
Data collection and refinement statistics.

Data set	Noxa1 SH3
Resolution range (Å)	50.00–1.885
Space group	$P2\ 2_12_1$
Unit cell dimensions (Å)	
a, b, c (Å)	30.596 49.014 72.868
α β, γ (°)	90.00 90.00 90.00
Unique reflections	9201
Completeness (%)	98.57/98.22
Mean $\langle I\rangle/\langle\sigma(I)\rangle$	27.2/2.22
Multiplicity	5/3.8
*R*merge (%)	10.6/64.2
B factor from Wilson plot ($Å^2$)	33.09
Refinement statistics*	
Resolution (Å)	40.68–1.885
R-factor/free *R*-factor (%)	0.2270/0.2555
Rms deviations from ideals	
Bond lengths (Å)/bond angles (°)	0.004/1.09
No. of atoms (protein/water)	909/48
B-values (all atoms)	
Average B-factor (protein/water, $Å^2$)	35.95/44.82
Ramachandran plot	
Residues in favored regions (%)	99.12
Residues in allowed region (%)	0.88
Residues in outliers (%)	0
PDB ID code	7CFZ

R factor is $\sum_{hkl}||F_o(hkl) - F_c(hkl)||/\sum_{hkl}F_o(hkl)$, where F_o and F_c are the observed and calculated structure factor amplitudes, respectively. The free R factor was calculated with 10% of data set not used in the refinement.

* Values in outer shell are for the highest shell with a resolution of 1.985–1.885 Å.

above a circular glass substrate (SiO_2). The diameter and thickness of the glass substrate was 35 mm and 1.8 mm, respectively. The spacing between adjacent silver electrodes on each plane was fixed at 2 mm. The V_{rms} was 1.17 kV and I_{rms} was 16 mA, and the discharge voltage was 1.08 kV, and having electrical energy of 3.88 J/s. The plasma on-time was 25 ms and the off-time was 150 ms.

The Soft Jet consists of two electrodes and a quartz tube. The hollow needle was used as high voltage electrode and covered with a quartz tube. The outer electrode acts as the ground electrode. The root-mean-square voltage and current were 0.48 kV and 160 mA, respectively, whereas the discharge voltage and energy were 1.6 kV and 6.88 J/s, respectively. The relative humidity (RH) was 50% (In/out Hygro-Thermometer, Model: TH01C, Company: Contriver Ltd, China) at 25 °C, close to the plasma jet. No chemical etching was observed on the walls of the stainless-steel needle after plasma treatment.

2.5. Circular dichroism (CD) spectroscopy

CD spectra of Noxa1 SH3 were measured using JASCO J-815 spectropolarimeter (Jasco, Tokyo, Japan), calibrated with ammonium D-10-camphorsulfonate at 290 nm and equipped with a thermostatically controlled cell holder attached to a water bath with an accuracy of ±0.1 °C. The samples were pre-equilibrated at the desired temperature for 15 min. The secondary structure of Noxa1 SH3 was monitored using a 1.0 mm path length cuvette. The concentration for Noxa1 SH3 was 0.5 mg/ml, and each spectrum was taken as the average of six spectra. Each sample spectrum was obtained by subtracting the appropriate blank without Noxa1 SH3 from the experimental protein spectrum. The percentages of secondary structures were calculated using K2D3 [39].

2.6. Fluorescence spectroscopy

A fluorescence assay was performed at 25 °C using an LS55 spectrophotometer (Perkin Elmer, Waltham, MA). The excitation wavelength was fixed at 280 nm for the overall fluorescence emission. The slit widths for excitation and emission were both set at 10 nm. The Noxa1 SH3 concentration was 1 mg/ml, and each spectrum was the average of six spectra with a 1 min incubation time for each increment.

2.7. pH and temperature measurement

After plasma exposure to the buffer solution (10 mM HEPES, 100 mM NaCl, 0.5 mM DTT, pH 6.0) for different time durations (1, 2, 3 or 5 min), the pH and temperature of the buffer were measured using a pH meter and Infrared (IR) camera. All measurements were carried out in triplicate.

2.8. Sample preparation

The protein was added to 2 ml screw-capped vials in buffer (10 mM HEPES, 100 mM NaCl, 0.5 mM DTT) at pH 6.0, kept on ice for 2 h to attain complete equilibrium after blending the solution. The samples were treated with pulsed DBD for 1, 3 and 5 min and with Soft Jet for 1, 2 and 3 min, at 5 mm distance from the plasma device, at a humidity of 50–60% RH, and were then incubated for 4 h in ice. Six samples were treated for each condition to minimize the error.

2.9. Molecular dynamics (MD) simulations

The MD simulations were performed using "Chain A" of Noxa1 SH3 (PDB 7CFZ), GROMACS 5.1.2 package [40] using the GROMOS54A7 force field [41]. The protein was solvated with water, described by the simple point charge (SPC) explicit solvent model [42]. Subsequently, to neutralize the system by Na^+ or Cl^- ions with replacing the water molecules. The system was energy minimized with the steepest descent method. The NPT equilibration was first carried out for 100 ns at 300 K and 1 bar by applying positional restraints (force constant of 1000 kJ mol^{-1} nm^{-2}) on the heavy atoms of the protein. This was done in order to keep the system as close as possible to its crystal structure. We employed V-rescale modified Berendsen thermostat with a time constant of 0.1 ps [43], Parrinello-Rahman barostat with a time constant of 2 ps [44], and isothermal compressibility of 4.5×10^{-5} bar^{-1} [45]. The cut-off radii of the van der Waals and Coulomb interaction were 1 nm. Additionally, the long-range electrostatic interaction was calculated by the PME (particle mesh Ewald summation) [46] and applying long-range dispersion corrections for both energy and pressure. After the equilibration, we performed the unrestrained (normal) MD simulations for another 300 ns, of which 50 ns was used for calculation of the average values. Thus, 250 ns time, out of the 300 ns MD simulations in the NPT ensemble, was used to equilibrate the protein system without applying any positional restraints. In all simulations, a time step of 2 fs was used. Finally, we calculated the root mean square deviation (RMSD) of the C_α atoms, the root mean square fluctuations (RMSFs) of the protein residues, the radius of gyration (Rg) and the solvent accessible surface area (SASA), and we applied principle component analysis (PCA), to check the stability, flexibility and surface area of the protein that is accessible to the solvent. Besides simulating the native Noxa1 SH3 structure in water, we also performed the same simulations to an oxidized form of Noxa1 SH3, to better understand the effect of plasma treatment (as example of external oxidative stress) on the Noxa1 SH3 stability. The structure of oxidized Noxa1 SH3 was based on the NMR spectra. More specifically, we modified the Gln413, Cys430, Cys441 and Val432 amino acids into 4-hydroxyglutamine, cysteic acid, and 3-hydroxyvaline, which are the most probable oxidized structures after plasma treatment based on literature [47]. For the oxidized Noxa1 SH3, the GROMOS54A7 force field parameters were obtained from [48,49].

2.10. Cell culture

Human A375 melanoma cells were maintained in Dulbecco's Minimum Essential Media (DMEM; Gibco), containing L-glutamine, supplemented with 10% heat-inactivated fetal bovine serum (FBS) and 0.5% penicillin/streptomycin at 37 °C, in a humidified 5% CO_2 atmosphere.

2.11. Cell viability

The day before treatment, 3×10^5 A375 cells were seeded out in a 6-well plate (Greiner). On the day of treatment, fresh DMEM medium was added to each well. The cells were treated for 5 min with either the pulsed DBD or Soft Jet. 24 h post treatment, the total well contents were collected in polystyrene round bottom test tubes (Greiner) and centrifuged for 5 min at 1500 rpm. The cells were resuspended in 1× Phosphate Buffered Saline (PBS; Gibco) and stained with propidium iodide. The cell viability was measured with the CytoFLEX flow cytometer (Beckman Coulter) and analyzed with FlowJo software.

2.12. Immunoblotting

The A375 cells were seeded and treated as described in this above Section 2.11. However, in this case, 6 h after treatment, the total well contents were centrifuged for 5 min at 15,000 rpm. The cell pellets were washed with 1× ice-cold PBS and centrifuged again for 5 min at 1500 rpm. Subsequently, the cell pellets were resuspended in lysis buffer (10 mM Tris-HCl pH 8; 1 mM EDTA; 400 mM NaCl; 0.1% NP-40), containing protease inhibitors. The total protein content was quantified using the colorimetric Pierce BCA Protein Assay kit (Thermo Scientific). Equal amounts of protein and volume was loaded onto a 12.5% polyacrylamide gel for NOX1 (65 kDa). After electrophoresis was

completed, the protein was transferred to a PVDF membrane and blocked in TBS-T (Tris-buffered Saline; 0.1% Tween-20), containing 5% non-fat dry milk, for 1 h at room temperature. After blocking, the membrane was incubated overnight at 4 °C with primary antibodies of the target proteins, diluted as 1:500, and 1:1000 for the GAPDH (Glyceraldehyde 3-phosphate dehydrogenase) loading control. After washing with TBS-T, the membrane was incubated with appropriate horseradish peroxidase (HRP)-conjugated secondary antibodies (antibodies were from Novus Biologicals for Nox1 (NBP1-31546)), diluted as 1: 2000 (anti-rabbit) for 1 h at room temperature. After washing, the membrane was incubated for 5 min with Immobilon Forte Western HRP substrate (Millipore) and the immunoreactive bands were subsequently visualized with a Syngene imager.

3. Results and discussion

3.1. Crystal structure of Noxa1 SH3$^{397–456}$

The Noxa1 SH3$^{397–456}$ protein was purified and the structure was analyzed by X-ray crystallography at 1.88 Å resolution. The resulting information is listed in Table 1. The space group was determined to be P22 (1)2(1), with two molecules in the asymmetric unit (see Fig. 2a and b). The protein contains 5-β strands, namely β1, β2, β3, β4 and β5, and one α-helix. These 5-β strands form two tightly packed anti-parallel β-sheets. Overall, Noxa1 SH3 forms a β-barrel structure that is a typical SH3 domain structure. The B-factor of Noxa1 SH3 molecule, having chain ID 'A and B' is plotted against the amino acid residue number in Fig. 2c. The B-factor indicates the true static or dynamic mobility of an atom, as well as where there are errors in model building. We can thus conclude that for Noxa1 SH3, the regions containing the 407–427, 430–438 and 440–448 residues seem to have high dynamic mobility. These regions with dynamic mobility may play a role in SH3 domain mediated protein-protein interaction networks [9]. Furthermore, we have compared our Noxa1 SH3 structure with other reported SH3 homologues, i.e., the PDB 5K28 structure [50]. A small difference was observed in RMSD values between Noxa1 SH3 and 5 K28, as shown in Table 2. However, the B-factor patterns of Noxa1 SH3 and 5K28 are quite similar to each other, as shown Fig. S1. We compared the Noxa1 SH3 structure and 5K28 structure, because we used the 5K28 protein (SH3 domain of MLK3) as a template model to build the new Noxa1 SH3 structure. The small difference in RMSD and B-factor pattern of Noxa1 SH3 and homologue protein MLK3 indicates that our method of model building and refinement is reasonable. The crystal structure of Noxa1 SH3 was deposited to the Protein Data Bank (PDB), with PDB ID 7CFZ. To test the effect of external oxidative stress on Noxa1 SH3, the protein was treated with both plasma devices, i.e., pulsed DBD and Soft Jet (simply called DBD and Jet) for different time intervals.

Table 2
Comparison of the RMSD values between Noxa1 SH3 and SH3 homologues (PDB 5K28).

RMSD	NOXA_SH3_A chain	NOXA_SH3_B chain	5K28_A chain
5K28_A chain	0.669 Å	0.623 Å	x
5K28_B chain	0.448 Å	0.457 Å	0.379 Å
NOXA_SH3_A chain	x	0.209 Å	x

Highlights

3.2. RONS concentrations in buffer after pulsed DBD and Soft Jet treatment

Both DBD and Jet were applied to a buffered aqueous solution (10 mM HEPES, 100 mM NaCl, 0.5 mM DTT, pH 6.0), producing various

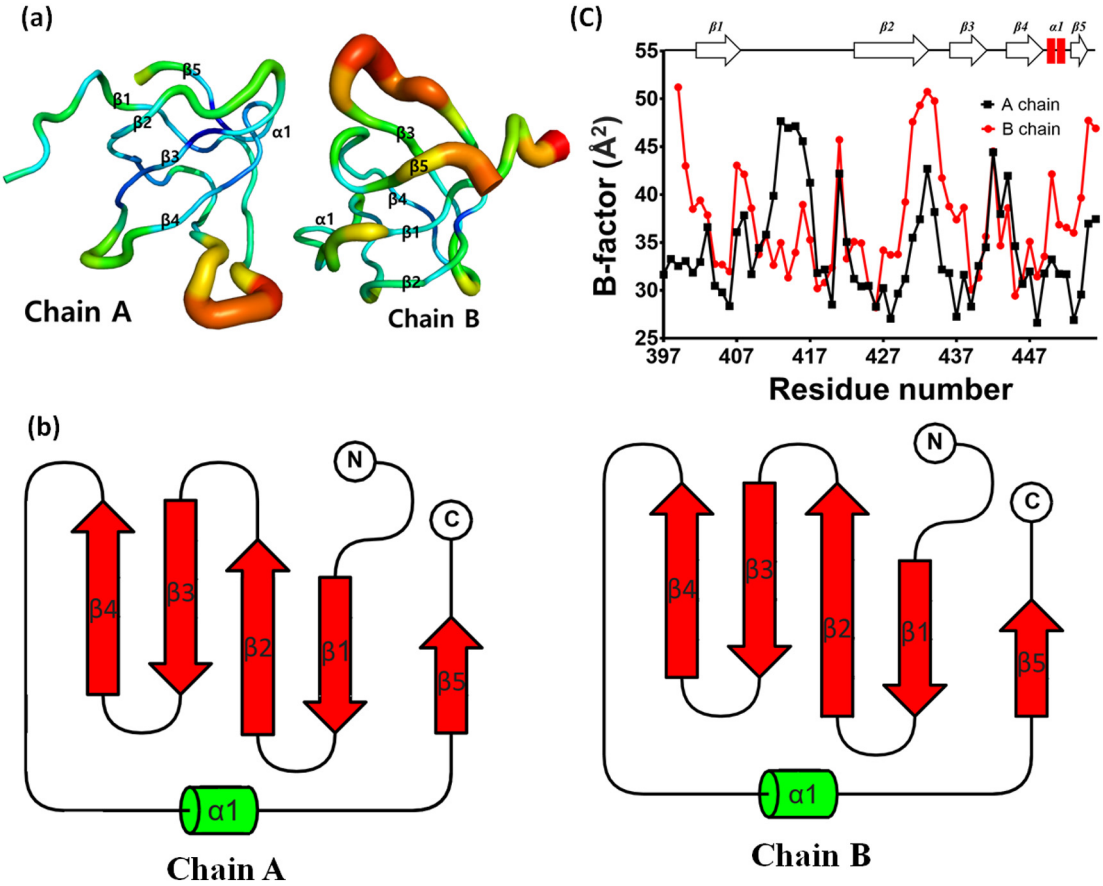

Fig. 2. (a) B-factor putty representation of two molecules in the asymmetric unit of Noxa1 SH3; (b) topology plot generated by TopDraw [54] and (c) B-factor of chain A and chain B in Noxa1 SH3 protein. 2D cartoon representatives of the secondary structures of Noxa1 SH3. (α helix as red bar, coil and turn as straight line, beta sheet as arrow). (For interpretation of the references to color in this figure legend, the reader is referred to the web version of this article.)

reactive oxygen and nitrogen species (RONS) in water, yielding so-called plasma-treated water (PTW). The concentrations of hydrogen peroxide (H_2O_2) and nitrite (NO_2^-) in the PTW were measured by titanyl ion and Griess reagent, respectively, as described elsewhere [51,52]. The OH intensity was measured using terephthalic acid (20 mM), by means of fluorescence spectroscopy, as also described earlier [31]. The concentration of H_2O_2 upon treatment with pulsed DBD for 1, 3 and 5 min was 6, 14 and 25 μM, whereas after Jet treatment for 1, 2 and 3 min, it was 9, 17 and 23 μM (Fig. 3a and b). Likewise, the concentration of NO_2^- was 8, 24 and 40 μM after DBD treatment for 1, 3 and 5 min, respectively, and 10, 21 and 29 μM after Jet treatment for 1, 2 and 3 min, respectively; see also Fig. 3a and b. Hence, these concentrations are slightly higher upon treatment with Jet than with DBD. On the other hand, the intensity of OH radicals was higher for DBD treatment compared to Jet treatment (see also Fig. 3c and d), qualitatively indicating that the OH concentration is higher upon treatment with DBD than with Jet.

The reason why we used different treatment times for DBD, and Jet is the following. Initially, we also treated the Noxa1 SH3 samples with the Jet for 1, 3 and 5 min, just like we applied for the DBD, but we observed that the protein structure was completely denatured for 5 min Jet treatment, i.e., the NMR peaks completely disappeared. Therefore, we decided to treat the Noxa1 SH3 protein for 1, 2 and 3 min of Jet treatment, and we applied the same treatment time for the buffer as well. We have not observed any aggregation in Noxa1 SH3 protein after both types of plasma treatment up to 5 min, but it may be possible for longer CAP treatment. Protein aggregation studies are interesting to understand the in vivo physiological processes, such as aging and cancer, so this would be of interest to study in future work.

3.3. CD and fluorescence analysis of Noxa1 SH3 before and after DBD and Jet plasma treatment

The Noxa1 SH3 protein was treated with DBD plasma for 1, 3 and 5 min in buffer. No pH and temperature changes were observed after DBD treatment. The CD spectrum in Fig. 4a shows that the control protein has 0.72% α-helix and 38.16% β-sheets, while after DBD treatment for 1, 3 and 5 min, the α-helix changes to 0.72, 0.59 and 0.48%, and the β-sheets change to 37.87, 38.24 and 38.4%, respectively. This shows that after 1 min DBD treatment, there is no change in α-helix structure, but there is a slight decrease in β-sheets. A longer treatment time results in a decrease of α-helix, but no significant change in β-sheets. This behavior of decrease in α-helix after plasma treatment is similar with previously reported work on different proteins [23,24].

The Noxa1 SH3 protein was also treated with the Jet for 1, 2 and 3 min in buffer, as shown in Fig. 4b. Again, no change in pH and temperature was observed upon treatment. The CD spectra in Fig. 4b again indicate 0.72% α-helix and 38.16% β-sheets in the control sample, while after Jet treatment for 1 and 2 min the α-helix changes to 0.71 and 0.81%, and the β-sheets change to 37.62 and 36.87%, respectively. We could not derive the change in the secondary structure of the protein after 3 min Jet treatment, due to protein denaturation. The CD data shows an increase in α-helix content after 2 min treatment, and a slight

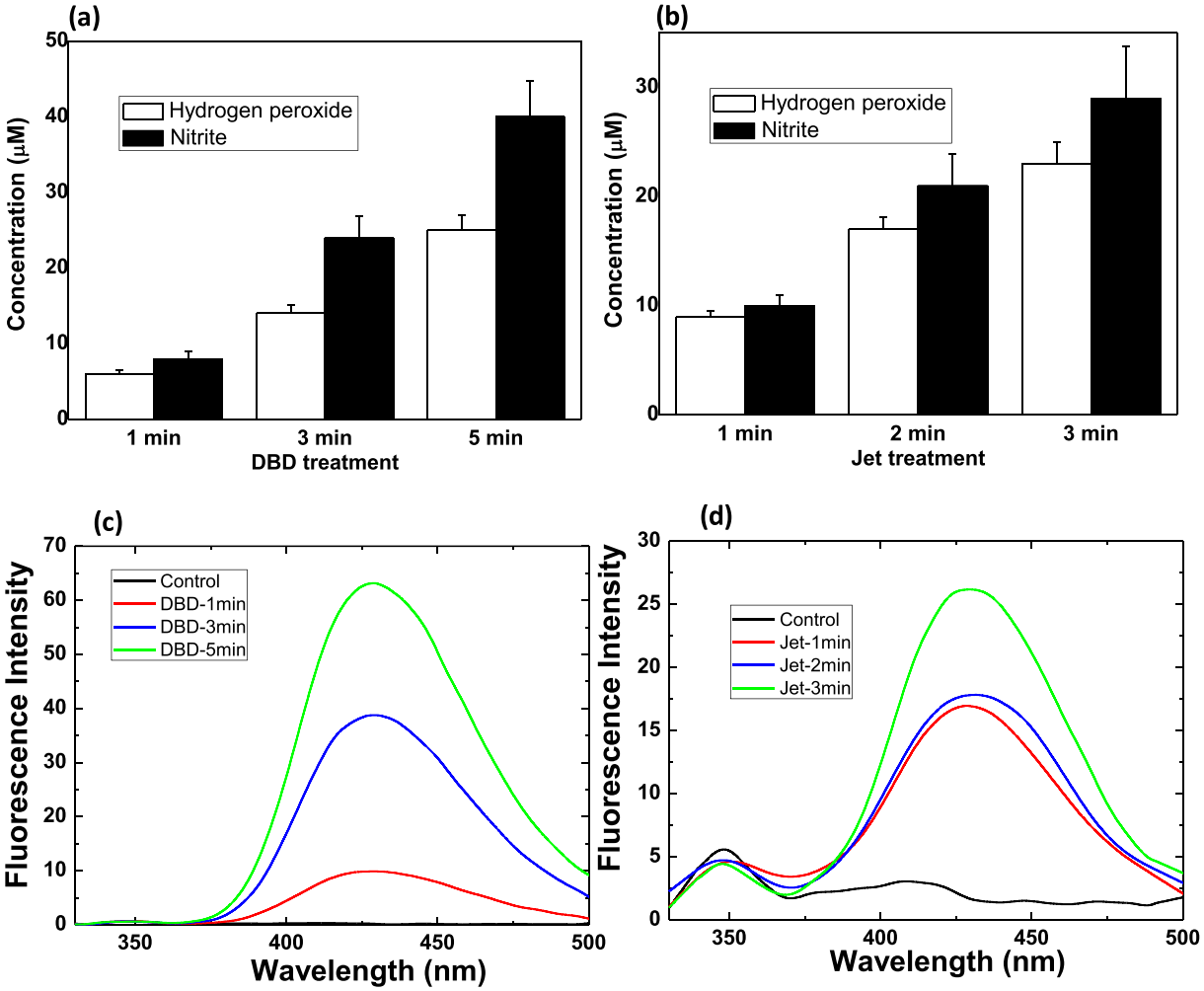

Fig. 3. (a) H_2O_2 and NO_2^- concentration after DBD treatment, (b) H_2O_2 and NO_2^- concentration after Jet treatment, (c) fluorescence intensity of OH radical production after pulsed DBD treatment, and (d) fluorescence intensity of OH radical production after Jet treatment, for different time intervals.

decrease in β-sheets content for 1- and 2-min treatment. In general, we can conclude that the Jet treatment has a stronger effect on the protein denaturation than DBD treatment. It might be due to the difference in the energy of Jet and DBD, see Section 2.4. The Jet energy was almost double the DBD energy, so it is logical that it has a stronger action than the DBD. In our previous work we also observed a similar behavior [21].

The intrinsic fluorescence spectrum of Noxa1 SH3 before and after DBD treatment is shown in Fig. 4c. Noxa1 SH3 contains one tryptophan (Trp) residue at 436, two tyrosine (Tyr) residues at 402 and 410, and two phenylalanine (Phe) residues at 448 and 452, which result in the intrinsic fluorescence spectra of Noxa1 SH3 protein. The intrinsic fluorescence in Noxa1 SH3 was mainly due to Trp and Tyr residues, while the influence of Phe is negligible due to its low absorptivity and low quantum yield [53]. At the same time Tyr has a comparable quantum yield to Trp. Noxa1 SH3 exhibits a maximum emission spectrum at 350 nm, but after DBD treatment for 1, 3 and 5 min, some quenching in fluorescence intensity was observed, as seen in Fig. 4c. Similar results are observed after Jet treatment for 1 and 2 min (Fig. 4d).

3.4. NMR analysis of Noxa1 SH3 before and after DBD and Jet treatments

To gain insight in the amino acids oxidized by DBD treatment, we performed $^{1}H—^{15}N$ NMR spectroscopy. The 2D HSQC spectra of Noxa1 SH3 were uniformly spread over the spectrum, which indicates the well-folded protein structure, see Fig. 5a. Peak shifts were noticed in the HSQC spectra after DBD treatment for different time intervals. The NMR peak shifts increase upon rising DBD treatment time from 1 to 5 min, due to the higher extent of amino acid oxidation. The maximum affected amino acids after DBD treatment were glutamine (Gln 413), aspartic acid (Asp 427), cysteine (Cys 430 and Cys 441), valine (Val 432), glycine (Gly 443 and Gly 446) and arginine (Arg 444), and their NMR peak shifts after DBD treatment for 1, 3 and 5 min are listed in Table S1.

Fig. 5b shows the NMR analysis of the Noxa1 SH3 protein after Jet treatment for 1, 2 and 3 min. We observed that many amino acid peaks were missing after the 3 min Jet treatment (cf. Fig. 5b), but the major modified amino acids were similar for both DBD and Jet plasma treatment, i.e., Gln 413, Asp 427, Cys 430, Val 432, Cys 441, Gly 443, Arg 444 and Gly 446. The peak shifts after Jet treatment for 1 and 2 min are listed in Table S2. Note that other amino acid peaks were also shifted after both DBD and Jet plasma treatments, but the amino acids listed in Tables S1 and S2 reflect the largest peak shifts after plasma treatment.

Our experimental studies show that the Noxa1 SH3 protein structure remains compact for 3 min DBD treatment. In contrast, the protein structure was denatured for 3 min Jet treatment. This may be due to the difference in energy of both plasma devices (DBD ≈ 3.88 J/s and Jet = 6.88 J/s), so after 3 min DBD treatment the energy was ~698 J, while for 3 min Jet treatment the energy was ~1238 J. The difference of ~540 J might be enough for this oxidized Noxa1 SH3 protein system to cross the energy barrier and change the transition state of the protein from folded to unfolded. Similarly, if we compare the structure modification in Jet treatment between 2 and 3 min, we also find an abrupt difference, which can again be related to the energy barrier, as the difference between 2 and 3 min Jet treatment was ~412 J. Hence, this might be the energy barrier to denature the oxidized Noxa1 SH3 protein structure. On the other hand, during plasma treatment many other factors also contribute to denaturation of the protein, and we would need further analysis to verify this assumption.

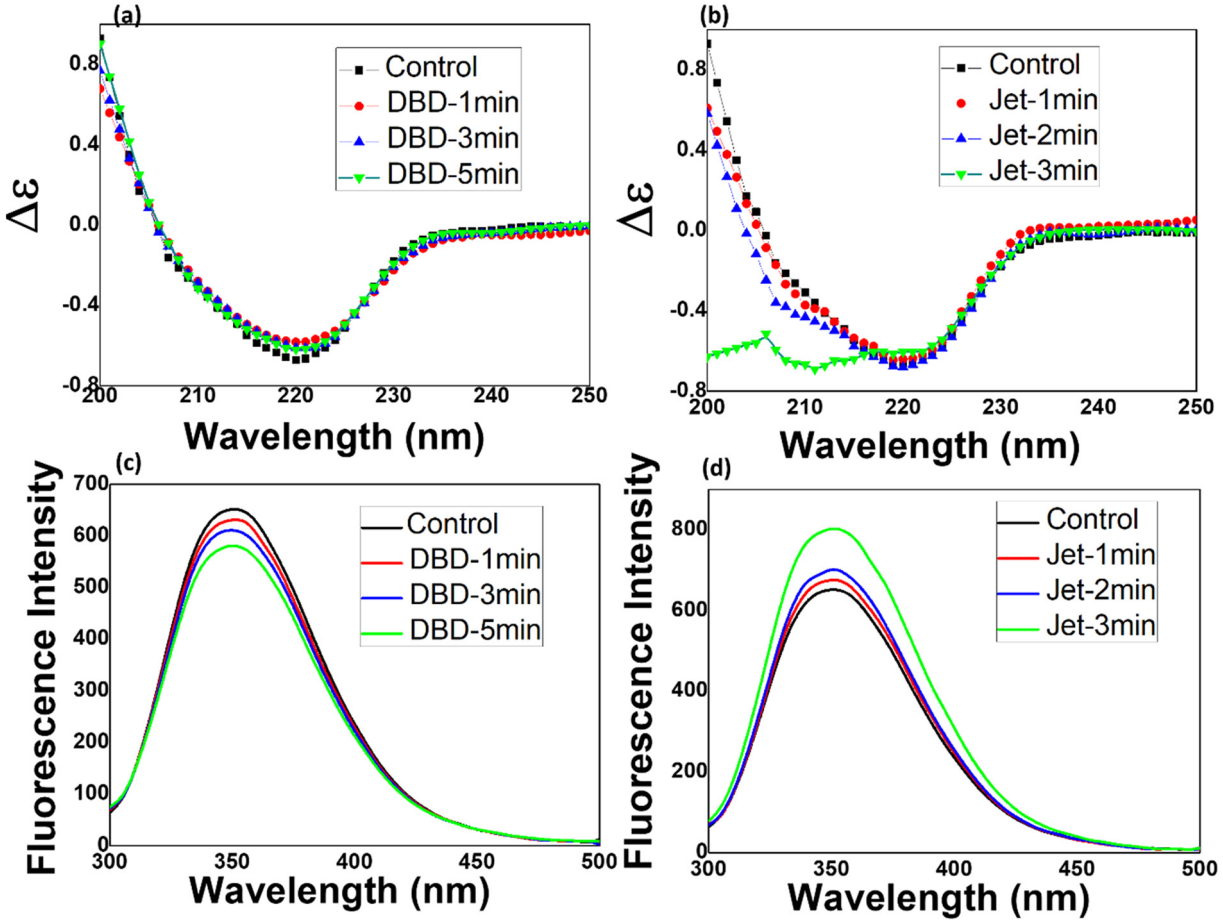

Fig. 4. (a, b) Far-UV CD spectra and (c, d) fluorescence spectra of Noxa1 SH3 protein before and after plasma treatment for different times, by pulsed DBD (a, c) or Soft Jet (b, d).

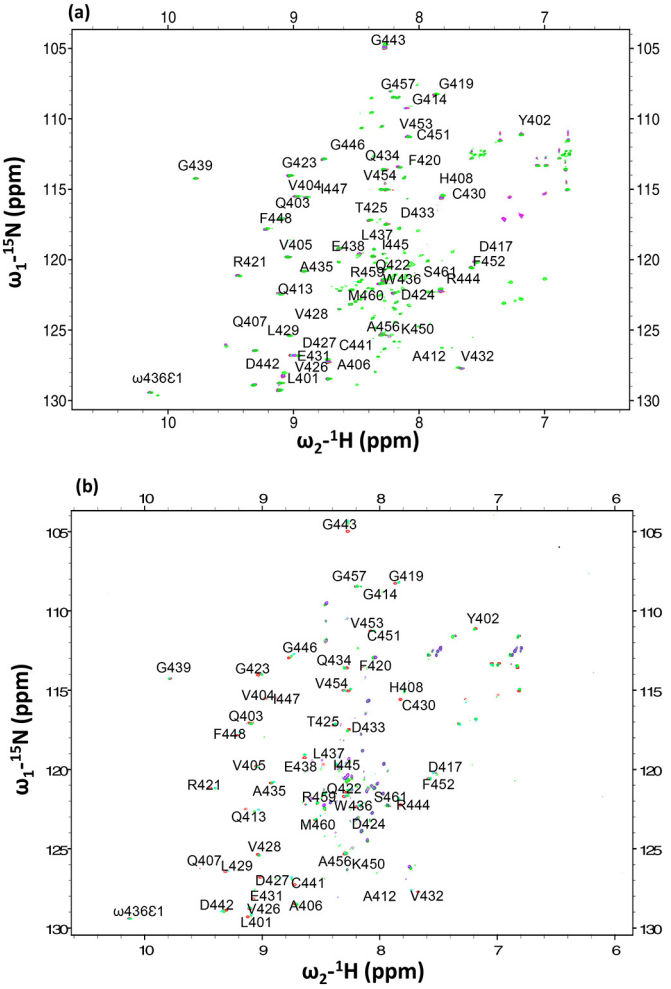

Fig. 5. $^{1}H—^{15}N$ NMR spectra of Noxa1 SH3 protein before [red color] and after pulsed DBD treatment (a) for 1 min (cyan), 3 min (pink) and 5 min (green), as well as after Soft Jet treatment (b) for 1 min (cyan), 2 min (green) and 3 min (blue). (For interpretation of the references to color in this figure legend, the reader is referred to the web version of this article.)

3.5. MD simulation of native and oxidized Noxa1 SH3 protein

Based on the NMR analysis and the previously reported oxidation state of amino acids by CAP [47], we performed MD simulations to calculate the RMSD, RMSF, Rg and SASA, and we carried out PCA for both native and oxidized Noxa1 SH3 protein, to evaluate the effect of plasma treatment, as external source of oxidative stress, on the stability and flexibility of the protein. As observed in Fig. 5 and Tables S1 and S2, several amino acids are modified after plasma treatment, but the force fields are not available for all of these amino acids, based on reference [47]. Therefore, we modified only a few amino acids, i.e., Gln413, Cys430, Cys441 and Val432. Gln was modified to 4-hydroxyglutamine, Cys to cysteic acid, and Val to 3-hydroxyvaline, before we performed the MD simulation for the oxidized Noxa1 SH3 protein.

Fig. 6a shows the RMSD of Cα atoms of both native and oxidized Noxa1 SH3 protein in water. The calculated average RMSD values were 0.18 ± 0.02 nm and 0.31 ± 0.03 nm for the native and oxidized protein, respectively. This indicates that the flexibility of Noxa1 SH3 increases upon oxidation. Fig. 6b illustrates the Rg of native and oxidized Noxa1 SH3. The average Rg was 1.06 ± 0.01 nm, and 1.07 ± 0.01 nm, for the native and oxidized protein, respectively. The average Rg value of native Noxa1 SH3 protein is slightly lower than oxidized Noxa1 SH3, which reveals that the native protein structure is marginally more compact than the oxidized protein structure. These results support the RMSD results that the flexibility of oxidized protein is more than the control protein. Fig. 6c depicts the RMSF as a function of residue number. The calculated average RMSF value for the native and oxidized protein was 0.13 ± 0.07 nm and 0.17 ± 0.10 nm, respectively. Similar to RMSD and Rg values, the RMSF value is less for the native Noxa1 SH3 protein than for the oxidized protein. This again supports our above explanation that after oxidation of the amino acids, the protein flexibility increases, and the compactness decreases, which results in more fluctuation of the oxidized protein residues. The residue 400–412 shows the high intensity for the oxidized Noxa1 SH3 protein; however, the peak at residue 413 nm disappeared, and the peak at residue 415 has shifted to residue 414. Similarly, the peak at residue 421 moved to residue 420. Similar peak shifts are observed between the residues 430–440, and no peak shifts were noted for residues 447–456 but they had higher intensity than the native protein. Summarized, the RMSD, Rg and RMSF values were higher for the oxidized protein, which supports our experimental data, where protein denaturation was observed after plasma treatment.

The PCA results provide information about the total phase space that each protein can occupy. The C_{α}-atomic positional fluctuations were found to be 0.75 and 1.59 nm^2 for the native and oxidized protein, respectively (cf. Fig. 7a). This also reveals that the structure of Noxa1 SH3 becomes unstable after oxidation of the amino acids. Fig. 7b shows the SASA results, which give information about the surface area of the protein that is accessible to the solvent. The average SASA values of the native and oxidized protein were 41.63 ± 1.1 and 41.60 ± 1.0 nm^2, respectively. SASA is a measure of the stability of the protein structure, as a higher stability result in a lower SASA value. We determined the SASA to check the average change in surface area of the protein in contact with water after oxidation. We have not observed any significant change in SASA values, which shows that the Noxa1 SH3 protein structure is stable after oxidation.

3.6. Effect of DBD and jet treatment on the expression of NOX1 in A375 cancer cells

To validate our hypothesis that plasma treatment can affect the expression of NOX1 in cancer cells, we performed western blotting analysis on A375 cancer cells. We treated the A375 cancer cells with DBD and Jet for 5 min. The cancer cell viability results reveal that cell death was higher for Jet treatment than for DBD treatment, as shown in Fig. 8a. The same behavior was observed during the cell-free treatment of Noxa1 protein, where Jet treatment denatured the protein to a larger extent in comparison to DBD treatment. The western blotting experiments (Fig. 8b) display a decrease in expression of NOX1 after Jet treatment. Thus, we may conclude that Jet treatment significantly affects the NOX1 function in A375 cancer cells, more than DBD treatment. Hence, this supports our hypothesis that the inactivation of NOX1 can be one possible pathway for anticancer treatment using plasma. However, we will check the interactions between Noxa1 and Noxo1 in cancer cells in our future study to support our hypothesis.

4. Conclusion

We compared structural distortion and oxidation in Noxa1 SH3 protein by two different plasma devices, i.e., DBD and Jet. Our CD, fluorescence, and NMR studies indicate that Noxa1 SH3 protein was oxidized by both types of plasma treatment. When comparing the plasma treatment by DBD and Jet, we found that Jet treatment results in intense denaturation action on Noxa1 SH3 protein as compared to DBD treatment for the same time interval, that was due to difference in the energy of the Jet and DBD treatment. In addition, Jet treatment yields a more pronounced drop in expression of NOX1, as well as more cancer cell death

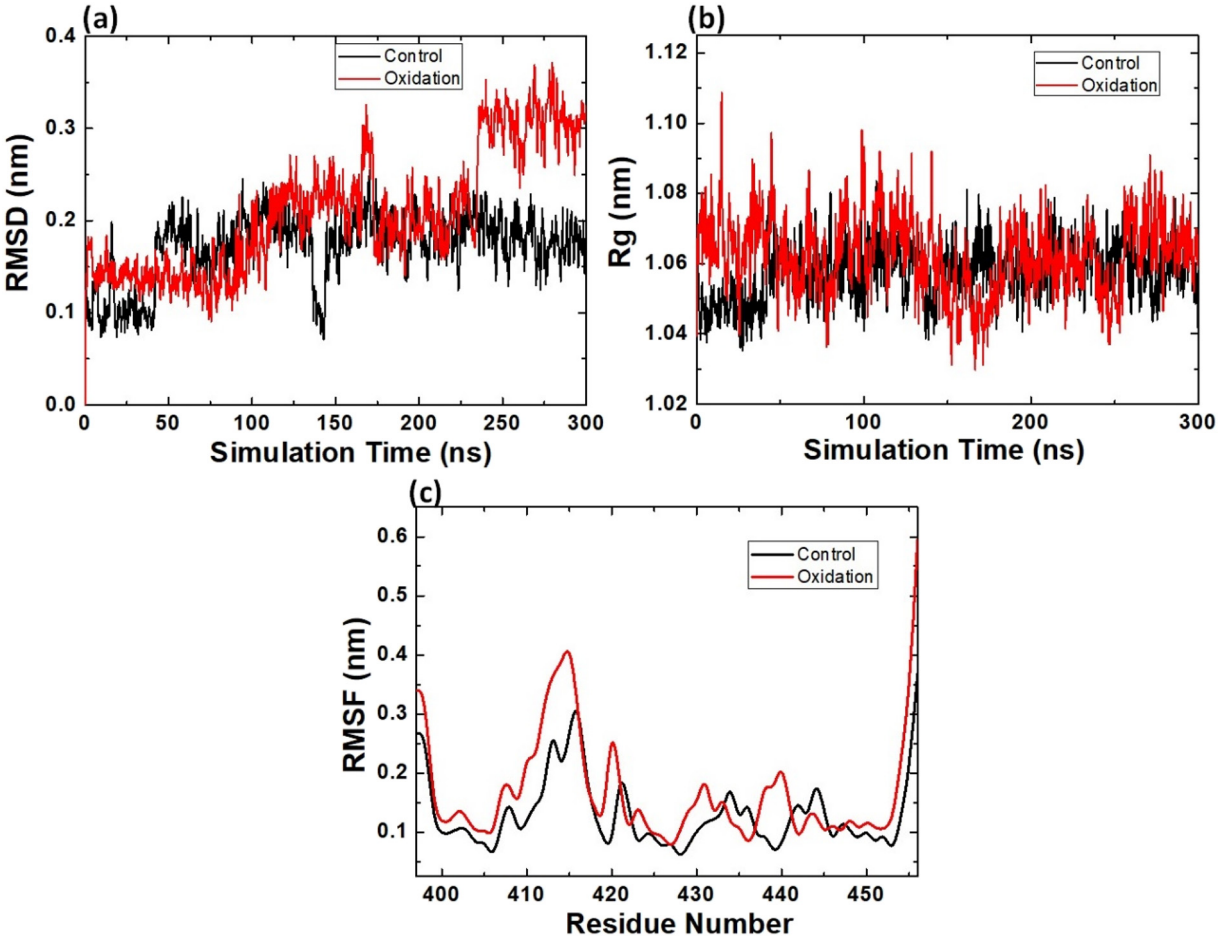

Fig. 6. MD simulation results of the native and oxidized Noxa1 SH3 protein. (a) Root mean square deviation (RMSD) of the C_α atoms, (b) radius of gyration (Rg), and (c) root mean square fluctuations (RMSFs).

with respect to DBD treatment. This indicates that deactivation of NOX1 upon plasma treatment could be one of the possible pathways for the anticancer effect of plasma. As CAP can also affect other proteins, further study is needed to understand how CAP can oxidize the Noxa1 protein in the presence of other proteins, as well as its interaction with Noxo1, both in cells or in cell-free conditions.

- Structural distortion of Noxa1 SH3 protein due to oxidative stress is created by cold atmospheric plasma.
- The crystal structure of Noxa1 SH3 protein is analyzed by X-ray crystallography.
- Soft Jet denatures the Noxa1 SH3 protein structure after 3 min treatment.

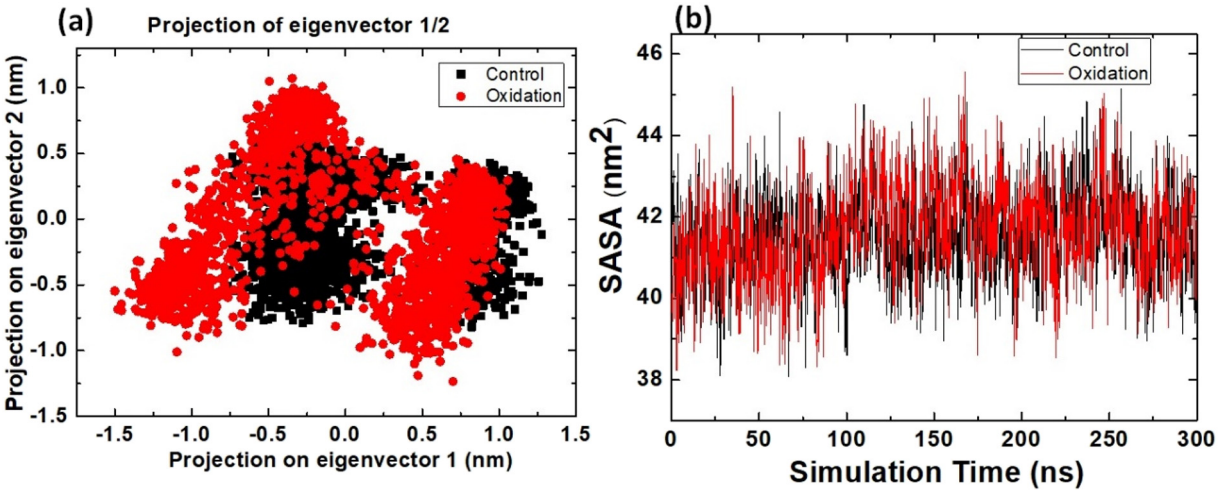

Fig. 7. (a) Principle component analysis (PCA) and (b) Solvent accessible surface area (SASA) results for the native and oxidized Noxa1 SH3 protein.

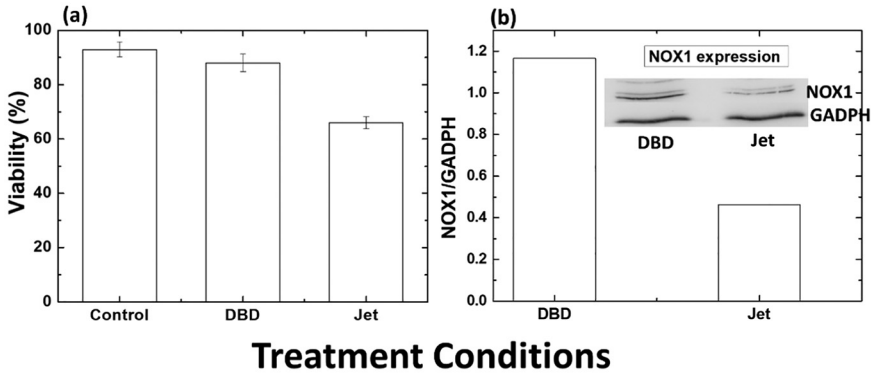

Fig. 8. (a) Viability of A375 cancer cells, and (b) Western blotting analysis of NOX1 of A375 cancer cells, after pulsed DBD and Soft Jet treatment.

Declaration of competing interest

The authors declare no conflict of interest.

Acknowledgments

We gratefully acknowledge the European Marie Skłodowska-Curie Individual Fellowship "Anticancer-PAM" within Horizon 2020 (grant number 743546). This work was also supported by JSPS-KAKENHI grant number 20K14454. Additionally, work was supported by several grants (2019M3A9F6021810, NRF-2017M3A9F6029753, NRF-2019M3E5D6063903 to W. Lee), Basic Science Research Program (NRF-2016R1A6A3A04010213 to J.H. Yun) through the National Research Foundation of Korea and in part by the Brain Korea 21 (BK21) PLUS program (J.H.P.). EHC is thankful to National Research Foundation (NRF) of Korea, funded by the Korea government (MSIT) under the grant number (NRF-2016K1A4A3914113). The computational work was carried out using the Turing HPC infrastructure at the CalcUA core facility of the Universiteit Antwerpen (UA), a division of the Flemish Supercomputer Center VSC, funded by the Hercules Foundation, the Flemish Government (department EWI) and the UA.

Appendix A. Supplementary data

Supplementary data to this article can be found online at https://doi.org/10.1016/j.ijbiomac.2020.09.120.

References

[1] J.D. Lambeth, NOX enzymes and the biology of reactive oxygen, Nat. Rev. Immunol. 4 (2004) 181–189, https://doi.org/10.1038/nri1312.
[2] H. Sumimoto, K. Miyano, R. Takeya, Molecular composition and regulation of the Nox family NAD(P)H oxidases, Biochem. Biophys. Res. Commun. 338 (2005) 677–686, https://doi.org/10.1016/j.bbrc.2005.08.210.
[3] S. Dutta, K. Rittinger, Regulation of NOXO1 activity through reversible interactions with p22phox and NOXA1, PLoS One 5 (2010), e10478, https://doi.org/10.1371/journal.pone.0010478.
[4] M. Skonieczna, T. Hejmo, A. Poterala-Hejmo, A. Cieslar-Pobuda, R.J. Buldak, NADPH oxidases: insights into selected functions and mechanisms of action in cancer and stem cells, Oxidative Med. Cell. Longev. 2017 (2017) 1–15, https://doi.org/10.1155/2017/9420539.
[5] T. Kamata, Roles of Nox1 and other Nox isoforms in cancer development, Cancer Sci. 100 (2009) 1382–1388, https://doi.org/10.1111/j.1349-7006.2009.01207.x.
[6] K. Bedard, K.-H. Krause, The NOX Family of ROS-generating NADPH oxidases: physiology and pathophysiology, Physiol. Rev. 87 (2007) 245–313, https://doi.org/10.1152/physrev.00044.2005.
[7] G. Cheng, Z. Cao, X. Xu, E.G.V. Meir, J.D. Lambeth, Homologs of gp91 phox : cloning and tissue expression of Nox3, Nox4, and Nox5, Gene 269 (2001) 131–140, https://doi.org/10.1016/S0378-1119(01)00449-8.
[8] D.I. Brown, K.K. Griendling, Nox proteins in signal transduction, Free Radic. Biol. Med. (2009)https://doi.org/10.1016/j.freeradbiomed.2009.07.023.
[9] P. Shrestha, J. hye Yun, Y.J. Ko, M. Kim, Y.S. Bae, W. Lee, C-terminal tail of NADPH oxidase organizer 1 (Noxo1) mediates interaction with NADPH oxidase activator (Noxa1) in the NOX1 complex, Biochem. Biophys. Res. Commun. 490 (2017) 594–600, https://doi.org/10.1016/j.bbrc.2017.06.083.
[10] N. Kumar, J.H. Park, S.N. Jeon, B.S. Park, E.H. Choi, P. Attri, The action of microsecond-pulsed plasma-activated media on the inactivation of human lung cancer cells, J. Phys. D. Appl. Phys. 49 (2016), 115401, https://doi.org/10.1088/0022-3727/49/11/115401.
[11] P. Attri, Cold atmospheric plasma activated solution: a new approach for cancer treatment, Anti Cancer Agents Med. Chem. 18 (2018) 768, https://doi.org/10.2174/1871520618061811212471 7.
[12] J. Hoon Park, N. Kumar, D. Hoon Park, M. Yusupov, E.C. Neyts, C.C.W. Verlackt, A. Bogaerts, M. Ho Kang, H. Sup Uhm, E. Ha Choi, P. Attri, A comparative study for the inactivation of multidrug resistance bacteria using dielectric barrier discharge and nano-second pulsed plasma, Sci. Rep. 5 (2015), 13849, https://doi.org/10.1038/srep13849.
[13] N. Eswaramoorthy, D.R. McKenzie, Plasma treatments of dressings for wound healing: a review, Biophys. Rev. 9 (2017) 895–917, https://doi.org/10.1007/s12551-017-0327-x.
[14] Lin Biscop, Loenhout Boxem, Deben Backer, Smits Dewilde, Bogaerts, Influence of cell type and culture medium on determining cancer selectivity of cold atmospheric plasma treatment, Cancers (Basel) 11 (2019) 1287, https://doi.org/10.3390/cancers11091287.
[15] D. Yan, W. Xu, X. Yao, L. Lin, J.H. Sherman, M. Keidar, The cell activation phenomena in the cold atmospheric plasma cancer treatment, Sci. Rep. 8 (2018), 15418, https://doi.org/10.1038/s41598-018-33914-w.
[16] W. Van Boxem, J. Van der Paal, Y. Gorbanev, S. Vanuytsel, E. Smits, S. Dewilde, A. Bogaerts, Anti-cancer capacity of plasma-treated PBS: effect of chemical composition on cancer cell cytotoxicity, Sci. Rep. 7 (2017), 16478, https://doi.org/10.1038/s41598-017-16758-8.
[17] P. Attri, A. Bogaerts, Perspectives of plasma-treated solutions as anticancer drugs, anticancer, Agents Med. Chem. 19 (2019) 436–438, https://doi.org/10.2174/1871520619041905211023 45.
[18] P. Attri, J.H. Park, A. Ali, E.H. Choi, How does plasma activated media treatment differ from direct cold plasma treatment? Anti Cancer Agents Med. Chem. 18 (2018) 805–814, https://doi.org/10.2174/1871520618666180406121734.
[19] A. Dubuc, P. Monsarrat, F. Virard, N. Merbahi, J.-P. Sarrette, S. Laurencin-Dalicieux, S. Cousty, Use of cold-atmospheric plasma in oncology: a concise systematic review, Ther. Adv. Med. Oncol. 10 (2018), 175883591878647, https://doi.org/10.1177/1758835918786475.
[20] G. Bauer, D. Sersenová, D.B. Graves, Z. Machala, Cold atmospheric plasma and plasma-activated medium trigger RONS-based tumor cell apoptosis, Sci. Rep. 9 (2019), 14210, https://doi.org/10.1038/s41598-019-50291-0.
[21] S. Choi, P. Attri, I. Lee, J. Oh, J.-H. Yun, J.H. Park, E.H. Choi, W. Lee, Structural and functional analysis of lysozyme after treatment with dielectric barrier discharge plasma and atmospheric pressure plasma jet, Sci. Rep. 7 (2017) 1027, https://doi.org/10.1038/s41598-017-01030-w.
[22] C. Bernard, A. Leduc, J. Barbeau, B. Saoudi, L. Yahia, G. De Crescenzo, Validation of cold plasma treatment for protein inactivation: a surface plasmon resonance-based biosensor study, J. Phys. D. Appl. Phys. 39 (2006) 3470–3478, https://doi.org/10.1088/0022-3727/39/16/S04.
[23] Z. Ke, Q. Huang, Inactivation and heme degradation of horseradish peroxidase induced by discharge plasma, Plasma Process. Polym. 10 (2013) 731–739, https://doi.org/10.1002/ppap.201300035.
[24] J.H. Park, M. Kim, M. Shiratani, A.E. Cho, E.H. Choi, P. Attri, Variation in structure of proteins by adjusting reactive oxygen and nitrogen species generated from dielectric barrier discharge jet, Sci. Rep. 6 (2016), 35883, https://doi.org/10.1038/srep35883.
[25] P. Attri, N. Kumar, J.H. Park, D.K. Yadav, S. Choi, H.S. Uhm, I.T. Kim, E.H. Choi, W. Lee, Influence of reactive species on the modification of biomolecules generated from the soft plasma, Sci. Rep. 5 (2015) 8221, https://doi.org/10.1038/srep08221.
[26] P. Attri, E.H. Choi, Influence of reactive oxygen species on the enzyme stability and activity in the presence of ionic liquids, PLoS One 8 (2013), e75096, https://doi.org/10.1371/journal.pone.0075096.
[27] P. Attri, P. Venkatesu, N. Kaushik, Y.G. Han, C.J. Nam, E.H. Choi, K.S. Kim, Effects of atmospheric-pressure non-thermal plasma jets on enzyme solutions, J. Korean Phys. Soc. 60 (2012) 959–964, https://doi.org/10.3938/jkps.60.959.

[28] P. Attri, P. Venkatesu, N. Kaushik, E.H. Choi, TMAO and sorbitol attenuate the deleterious action of atmospheric pressure non-thermal jet plasma on α-chymotrypsin, RSC Adv. 2 (2012) 7146, https://doi.org/10.1039/c2ra20085f.
[29] H.-P. Li, L.-Y. Wang, G. Li, L.-H. Jin, P.-S. Le, H.-X. Zhao, X.-H. Xing, C.-Y. Bao, Manipulation of lipase activity by the helium radio-frequency, atmospheric-pressure glow discharge plasma jet, Plasma Process. Polym. 8 (2011) 224–229, https://doi.org/10.1002/ppap.201000035.
[30] P. Attri, J. Han, S. Choi, E.H. Choi, A. Bogaerts, W. Lee, CAP modifies the structure of a model protein from thermophilic bacteria: mechanisms of CAP-mediated inactivation, Sci. Rep. 8 (2018), 10218, https://doi.org/10.1038/s41598-018-28600-w.
[31] P. Attri, T. Sarinont, M. Kim, T. Amano, K. Koga, A.E. Cho, E.H. Choi, M. Shiratani, Influence of ionic liquid and ionic salt on protein against the reactive species generated using dielectric barrier discharge plasma, Sci. Rep. 5 (2015) 17781, https://doi.org/10.1038/srep17781.
[32] P. Attri, J. Razzokov, M. Yusupov, K. Koga, M. Shiratani, A. Bogaerts, Influence of osmolytes and ionic liquids on the Bacteriorhodopsin structure in the absence and presence of oxidative stress: a combined experimental and computational study, Int. J. Biol. Macromol. 148 (2020) 657–665, https://doi.org/10.1016/j.ijbiomac.2020.01.179.
[33] D. Weber, M.J. Davies, T. Grune, Determination of protein carbonyls in plasma, cell extracts, tissue homogenates, isolated proteins: focus on sample preparation and derivatization conditions, Redox Biol. 5 (2015) 367–380, https://doi.org/10.1016/j.redox.2015.06.005.
[34] Z. Otwinowski, W. Minor, [20] Processing of X-ray diffraction data collected in oscillation mode, Methods Enzymol 1997, pp. 307–326, https://doi.org/10.1016/S0076-6879(97)76066-X.
[35] A.J. McCoy, R.W. Grosse-Kunstleve, P.D. Adams, M.D. Winn, L.C. Storoni, R.J. Read, Phaser crystallographic software, J. Appl. Crystallogr. 40 (2007) 658–674, https://doi.org/10.1107/S0021889807021206.
[36] N. 4 Collaborative Computational Project, The CCP4 suite: programs for protein crystallography, Acta Crystallogr. Sect. D Biol. Crystallogr. 50 (1994) 760–763, https://doi.org/10.1107/S0907444994003112.
[37] P.V. Afonine, R.W. Grosse-Kunstleve, N. Echols, J.J. Headd, N.W. Moriarty, M. Mustyakimov, T.C. Terwilliger, A. Urzhumtsev, P.H. Zwart, P.D. Adams, Towards automated crystallographic structure refinement with phenix.refine, Acta Crystallogr. Sect. D Biol. Crystallogr. 68 (2012) 352–367, https://doi.org/10.1107/S0907444912001308.
[38] P. Emsley, K. Cowtan, Coot: model-building tools for molecular graphics, Acta Crystallogr. Sect. D Biol. Crystallogr. 60 (2004) 2126–2132, https://doi.org/10.1107/S0907444904019158.
[39] C. Louis-Jeune, M.A. Andrade-Navarro, C. Perez-Iratxeta, Prediction of protein secondary structure from circular dichroism using theoretically derived spectra, Prot. Struct. Funct. Bioinform. 80 (2012) 374–381, https://doi.org/10.1002/prot.23188.
[40] G.M.J. Abraham, D. van der Spoel, E. Lindahl, B. Hess, Development Team, GROMACS user man. version 5.1.2, www.gromacs.org 2016.
[41] N. Schmid, et al., A.P. Eichenberger, A. Choutko, S. Riniker, M. Winger, A.E. Mark, W.F. van Gunsteren, Definition and testing of the GROMOS force-field versions 54A7 and 54B7, Eur. Biophys. J. 40 (2011) 843–856, https://doi.org/10.1007/s00249-011-0700-9.
[42] H.J.C. Berendsen, J.P.M. Postma, W.F. van Gunsteren, J. Hermans, Interaction Models for Water in Relation to Protein Hydration, 1981 331–342, https://doi.org/10.1007/978-94-015-7658-1_21.
[43] G. Bussi, D. Donadio, M. Parrinello, Canonical sampling through velocity rescaling, J. Chem. Phys. 126 (2007), 014101, https://doi.org/10.1063/1.2408420.
[44] M. Parrinello, A. Rahman, Polymorphic transitions in single crystals: A new molecular dynamics method, J. Appl. Phys. 52 (1981) 7182–7190, https://doi.org/10.1063/1.328693.
[45] H.J.C. Berendsen, J.P.M. Postma, W.F. van Gunsteren, A. DiNola, J.R. Haak, Molecular dynamics with coupling to an external bath, J. Chem. Phys. 81 (1984) 3684–3690, https://doi.org/10.1063/1.448118.
[46] T. Darden, D. York, L. Pedersen, Particle mesh Ewald: an N·log(N) method for Ewald sums in large systems, J. Chem. Phys. 98 (1993) 10089–10092, https://doi.org/10.1063/1.464397.
[47] E. Takai, T. Kitamura, J. Kuwabara, S. Ikawa, S. Yoshizawa, K. Shiraki, H. Kawasaki, R. Arakawa, K. Kitano, Chemical modification of amino acids by atmospheric-pressure cold plasma in aqueous solution, J. Phys. D. Appl. Phys. 47 (2014), 285403, https://doi.org/10.1088/0022-3727/47/28/285403.
[48] C. Margreitter, D. Petrov, B. Zagrovic, Vienna-PTM web server: a toolkit for MD simulations of protein post-translational modifications, Nucleic Acids Res. 41 (2013) W422–W426, https://doi.org/10.1093/nar/gkt416.
[49] C. Margreitter, M.M. Reif, C. Oostenbrink, Update on phosphate and charged post-translationally modified amino acid parameters in the GROMOS force field, J. Comput. Chem. (2017)https://doi.org/10.1002/jcc.24733.
[50] M.E. Kokoszka, S.L. Kall, S. Khosla, J.E. McGinnis, A. Lavie, B.K. Kay, Identification of two distinct peptide-binding pockets in the SH3 domain of human mixed-lineage kinase 3, J. Biol. Chem. 293 (2018) 13553–13565, https://doi.org/10.1074/jbc.RA117.000262.
[51] P. Attri, Y.H. Kim, D.H. Park, J.H. Park, Y.J. Hong, H.S. Uhm, K.-N. Kim, A. Fridman, E.H. Choi, Generation mechanism of hydroxyl radical species and its lifetime prediction during the plasma-initiated ultraviolet (UV) photolysis, Sci. Rep. 5 (2015) 9332, https://doi.org/10.1038/srep09332.
[52] P. Attri, M. Yusupov, J.H. Park, L.P. Lingamdinne, J.R. Koduru, M. Shiratani, E.H. Choi, A. Bogaerts, Mechanism and comparison of needle-type non-thermal direct and indirect atmospheric pressure plasma jets on the degradation of dyes, Sci. Rep. 6 (2016), 34419, https://doi.org/10.1038/srep34419.
[53] A. Ghisaidoobe, S. Chung, Intrinsic tryptophan fluorescence in the detection and analysis of proteins: a focus on Förster resonance energy transfer techniques, Int. J. Mol. Sci. 15 (2014) 22518–22538, https://doi.org/10.3390/ijms151222518.
[54] C.S. Bond, TopDraw: a sketchpad for protein structure topology cartoons, Bioinformatics 19 (2003) 311–312, https://doi.org/10.1093/bioinformatics/19.2.311.